

# Lab on a Chip

Accepted Manuscript



This is an *Accepted Manuscript*, which has been through the Royal Society of Chemistry peer review process and has been accepted for publication.

*Accepted Manuscripts* are published online shortly after acceptance, before technical editing, formatting and proof reading. Using this free service, authors can make their results available to the community, in citable form, before we publish the edited article. We will replace this *Accepted Manuscript* with the edited and formatted *Advance Article* as soon as it is available.

You can find more information about *Accepted Manuscripts* in the [Information for Authors](#).

Please note that technical editing may introduce minor changes to the text and/or graphics, which may alter content. The journal's standard [Terms & Conditions](#) and the [Ethical guidelines](#) still apply. In no event shall the Royal Society of Chemistry be held responsible for any errors or omissions in this *Accepted Manuscript* or any consequences arising from the use of any information it contains.

## PAPER

## Cooperative roles of biological flow and surface topography in guiding sperm migration revealed by a microfluidic model

Cite this: DOI: 10.1039/x0xx00000x

Received 00th January 2012,  
Accepted 00th January 2012

DOI: 10.1039/x0xx00000x

[www.rsc.org/](http://www.rsc.org/)

Chih-kuan Tung,<sup>a</sup> Florencia Ardon,<sup>b</sup> Alyssa Fiore,<sup>a</sup> Susan S. Suarez,<sup>b</sup> and Mingming Wu<sup>a</sup>

Successful reproduction in mammals requires sperm to swim against a fluid flow and through the long and complex female reproductive tract before reaching the egg in the oviduct. Millions of them do not make it. Despite the clinical importance, the roles played in sperm migration by the diverse biophysical and biochemical microenvironments within the reproductive tract are largely unknown. In this article, we present the development of a double layer microfluidic device that recreates two important biophysical environments within female reproductive tract: fluid flow and surface topography. The unique feature of the device is that it enables one to study the cooperative roles of fluid flow and surface topography in guiding sperm migration. Using bull sperm as a model system, we found that microfluidic grooves embedded on a channel surface facilitate sperm migration against fluid flows. These findings suggest ways to design *in vitro* fertilization devices to treat infertility and to develop non-invasive contraceptives that use microarchitectural design to entrap sperm.

## Introduction

In mammals, successful reproduction requires sperm to migrate tens of thousands of its body length through the female reproductive tract to reach the egg.<sup>1-3</sup> Despite the clinical importance, little is known about how sperm enter the cervix, pass through the uterotubal junction and reach the oviduct, in particular, in the presence of a flow that is opposite to the sperm swimming direction.<sup>4,5</sup> What we do know tells us that fertilization does not succeed merely due to the insemination of massive number of sperm, but rather depends on interactions of the sperm with the reproductive tract.<sup>4,6</sup> It is therefore important to explore roles of biochemical and biophysical environments within the reproductive tract in guiding mammalian sperm migration.

Extensive work has been carried out to investigate the roles of biochemical factors secreted within the female reproductive tract in guiding mammalian sperm migration.<sup>7-11</sup> Mammalian sperm share major features with their evolutionary ancestors, particularly the structure of the motor in the sperm tail,<sup>3</sup> such that sea urchin sperm have been used by many as a model for studying sperm movement and fertilization. Sperm of the sea urchin *Arbacia punctulata* are extremely sensitive to a chemoattractant that is secreted by the eggs.<sup>11, 12</sup> Strong experimental results, including those of our own group, have demonstrated that sea urchin sperm are chemotactic along a gradient of egg chemoattractant.<sup>13</sup> Consequently, extensive work has been carried out to seek similar sperm chemoattractants in mammals,<sup>7-11</sup> with some success. Nevertheless, it is not clear whether chemotaxis is a universal mechanism for guiding mammalian sperm migration or, if it exists, whether it is the sole mechanism of sperm guidance. This is not surprising, because the environment for the interactions of sea urchin sperm and eggs is dramatically different from that of mammalian sperm and eggs. In the case of sea urchins, the sperm must reach the egg in a few seconds before the moving water sweeps away the egg; while

in mammals, the female reproductive tract provides a well-defined, and yet complex environment for the sperm to swim through.<sup>1, 4</sup>

Increasingly, evidence has emerged that biophysical factors within the female reproductive tract play important roles in guiding mammalian sperm migration. These include surface topography<sup>14-16</sup> and fluid flow.<sup>5, 17</sup> Detailed examination of the histological architecture of the bovine cervix revealed microgrooves of about 10-20  $\mu\text{m}$  in width embedded along the mucosal surfaces of the bovine cervix (See Fig. 1) and it was proposed that the microgrooves provide preferential passageways for sperm to travel from the vagina into the uterus.<sup>5</sup> Similar microgrooves are also apparent in frozen sections of the bovine uterotubal junction, which forms a gateway between the uterus and oviduct.<sup>4</sup> This is consistent with reports that implicate physical boundaries in guiding sperm migration; that is, the observation that sperm tend to swim along and remain near the walls of a container or channel.<sup>15, 16, 18-20</sup> Another important biophysical factor is the fluid flow. At the time of insemination, cell secretion, ciliary beating, and muscle contraction within female tract create a fluid flow that is opposite to the swimming direction of the sperm.<sup>3, 5</sup> In the mouse oviduct, the average flow rate has been reported to be  $18.0 \pm 1.6 \mu\text{m s}^{-1}$  at the time of mating.<sup>5</sup> The question is whether the sperm will be swept away by the fluid flows, or rather swim against them.<sup>17</sup> Recent work has shown that sperm,<sup>5, 17, 21</sup> as well as other microswimmers such as *Escherichia coli*,<sup>22</sup> have a tendency to swim against the flow in certain ranges of flow speed. This behaviour is known as “rheotaxis”. Despite the implications of surface topography and fluid flows in guiding sperm migration, the cooperative roles of these important factors remain to be investigated.<sup>17</sup> This is, in part, hindered by the lack of experimental tools for modelling the complex biophysical environment of reproductive tract.

In this paper, we present a microfluidic model that provides well-defined fluid flow and, at the same time, channel surface topography that recreates the essential biophysical environmental cues

within the female reproductive tract. Using this model, we studied cooperative roles of fluid flow and topography in guiding sperm cell migration, and demonstrated that microfabricated grooves in channel surfaces facilitate sperm cell migration against a flow. This model is straightforward to implement, allows for parallel experiments (currently 6 of them, can be extended easily to 12 or more). The knowledge gained here will have direct applications in designing efficient *in vitro* fertilization systems<sup>23, 24</sup> and contraceptives that use microarchitecture to trap sperm. Furthermore, these devices can be extended to study the mechanisms of migration of microswimmers that infect the female reproductive tract, such as bacteria and the parasites that cause trichomoniasis.<sup>25, 26</sup> It should be noted that a number of groups have developed microfluidic systems for application to assisted reproductive technologies,<sup>27, 28</sup> including the selection of motile sperm,<sup>21</sup> prevention of polyspermic penetration,<sup>29</sup> and embryo culture.<sup>30</sup>

## Experimental Methods

### Device fabrication and assembly

The microfluidic device was fabricated using standard soft lithography technique. The silicon master was first made using a two-step deep silicon etching process, and the final microfluidic device was replicated from the silicon master using the PDMS stamping technique.

The fabrication of the negative silicon master mould was done at Cornell NanoScale Science & Technology Facility (CNF). Two deep silicon etching steps were masked by combinations between silicon oxide and photoresist to achieve (i) the 20  $\mu\text{m}$  deep grooves, and (ii) the 120  $\mu\text{m}$  deep main channel. The detailed procedures were as follows: 0.5  $\mu\text{m}$  of silicon oxide was first deposited onto a 100 mm silicon wafer (SEMI standard, SSP, 0.5 mm thick) by plasma enhanced chemical vapour deposition (PECVD, GSI) at 400°C. Photoresist (Microposit S1813, Shipley,

Marlborough, MA, USA) was then spun onto the surface (3000 rpm for 45 s), soft baked at 115 °C for one min, and then exposed ( $128.7 \text{ mJ cm}^{-2}$ ) on a contact aligner (Karl Suss MA/BA 6 aligner, Suss MicroTec, Garching, Germany, soft contact mode). After developing the resist (60 s MF-321 development, HamaTech-Steag Wafer Processor, Santa Clara, CA, USA), the wafer was then etched by a Reactive Ion Etcher (RIE, Oxford PlasmaLab 80+ RIE system, Oxford Instruments, Wiesbaden, Germany) using a combination of  $\text{CHF}_3/\text{O}_2$  and  $\text{CF}_4$  to etch through the PECVD oxide. Once the oxide was etched through, the resist was removed in a hot bath (Resist Hot Strip Bath, with propylene glycol, NMP, TMAH heated at 60 °C) for 30 min.

The second layer that defined the main flow channels was made onto the silicon wafer with the same contact lithography method, except with a different photoresist (Megaposit SPR2 20-7.0, Shipley, 2500 rpm, 40 s), exposure dosage ( $1.05 \text{ J cm}^{-2}$ ), an additional post-exposure wait time (90 min), and developer (AZ 726 MIF). The same RIE method and instrument were used to etch through the oxide, followed by a 100  $\mu\text{m}$  Botsch deep silicon etching process (Unaxis 770 Deep Silicon Etcher, Oerlikon, Pfäffikon, Switzerland). We then stripped the photoresist by two steps, first immersing the wafer in the hot strip for 90 min, followed by a 90 s oxygen plasma ashing (AURA 1000 Resist Strip, GaSonic, San Jose, CA, USA), since some resist might have been hardened in the DRIE process. After the thorough stripping processes, the same deep silicon etching was used to etch the wafer for another 20  $\mu\text{m}$ , which was now masked by the oxide. The wafer was next treated with (1H,1H,2H,2H-Perfluorooctyl) Trichlorosilane, or FOTS, using a single layer vapour deposition method (Molecular Vapor Deposition, Applied Microstructures, San Jose, CA, USA) to ensure the easy release of PDMS from the silicon master.

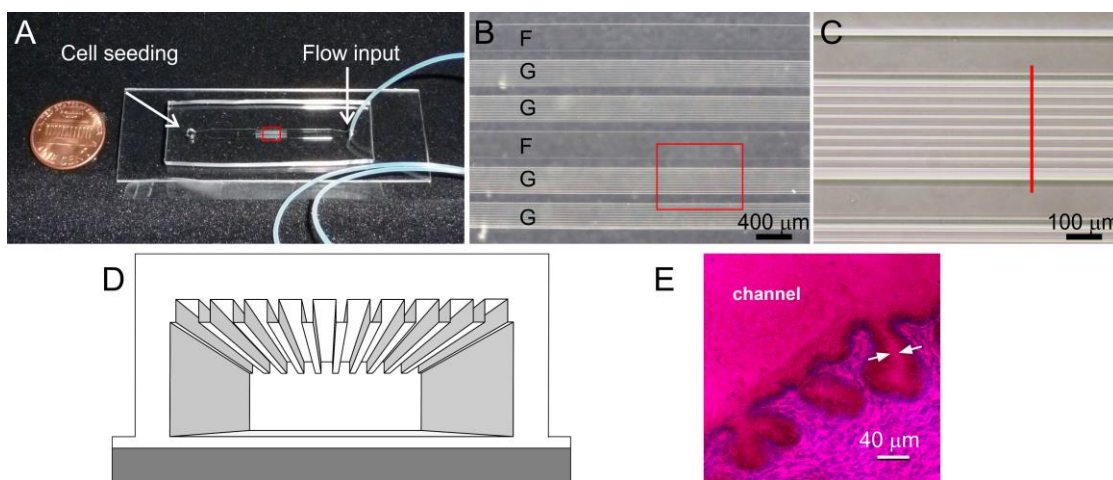


**Fig. 1 A double layer microfluidic device for modelling the biophysical environment of sperm in the female reproductive tract.** **A.** Image of a PDMS device bonded onto a PDMS coated glass slide (1" x 3"), with a port on the left for sperm seeding, and a port on the right for flow input. **B.** A close up image of the 6 sets of channels in the centre, four with grooves (noted with G) and two without (noted with F). **C.** A close up image of a G channel showing a set of nine 20  $\mu\text{m}$  wide and 20  $\mu\text{m}$  deep grooves. The G channel is 300  $\mu\text{m}$  wide and 120  $\mu\text{m}$  in height. **D.** A 3D drawing illustrating the cross section of the G channel. Drawing not to scale. **E.** A micrograph of a frozen tissue section of the bovine cervix, stained with PAS/hematoxylin. Micrometer size grooves are seen along the main channel wall. The white arrows indicate one of the microgrooves. Detailed methods in Suarez *et al.*<sup>4</sup>

We next prepared the PDMS piece, and bonded it onto a PDMS coated glass slide. 9:1 base to curing agent PDMS (SYLGARD 184 Silicone Elastomer Kit, Dow Corning, Midland, MI, USA) procedures were used for making a PDMS replica from the silicon master, and a PDMS coated glass slide from a flat glass surface. After curing, one 2 mm hole and one 1 mm hole were punched using biopsy punches (Miltex Inc, York, PA, USA), in order to provide access to the channels. The PDMS piece and the PDMS coated glass slide were next treated with oxygen plasma for one min on a high power setting using a plasma cleaner (Harrick Plasma Cleaner PDC-001, Harrick Plasma, Ithaca, NY, USA). The PDMS device was next sandwiched between a Plexiglas manifold and the PDMS coated glass slide for 10 min to ensure the quality of bonding, with the PDMS coated side touching the structured side of the PDMS device. The bonded device was then released from the Plexiglas manifold, and tubing (Weico Wire & Cable, ETT-24, Edgewood, NY, USA) was inserted into the 1 mm hole to provide a flow, as shown in Fig. 1A.

The assembly was next wetted with de-ionized water, and autoclaved immersed in DI water to ensure sterile conditions, and remove air bubbles.

### Flow control and measurements

Fluid flows within the microfluidic channels were generated by a syringe pump (KDS-230, KD Scientific, Holliston, MA, USA), and 1 mL syringes (BD, Franklin Lakes, NJ, USA). The flows were measured using a particle tracking method with 0.51  $\mu\text{m}$  diameter fluorescent beads (Dragon Green, Bangs Laboratories, Fishers, IN, USA). Images of the fluorescent beads were taken with short exposure time (10 ms) at 30 frames  $\text{s}^{-1}$  with flow rates ranging from 0-5  $\mu\text{L min}^{-1}$ . We then tracked each bead's location over time to obtain the flow speeds.

Since the spatial resolution of particle tracing is limited by the optical resolution of the microscope, especially in the  $z$  direction, we used COMSOL Multiphysics 4.3 to obtain finer structures of the flow profiles, and compared with the experimental measurements. The Navier-Stokes Equation was solved to calculate the flow field using a 3D laminar flow model.

### Imaging and data analysis

Flow characterization images were taken by an EMCCD camera (Cascade S128, Roper Scientific, Tucson, AZ, USA) in conjunction with an epi-fluorescence microscope (IX-81, Olympus America, Center Valley, PA, USA) with a 20X objective (Olympus).

Sperm images were taken by a NEO sCMOS camera (DC-152Q-C00-FI, Andor Technology, Belfast, UK) in conjunction with an inverted phase contrast microscope (Axiovert 35, Carl Zeiss Microscopy, Thornwood, NY, USA) with a 10X objective. The images were recorded using NIS Elements software (Nikon Instruments, Inc., Melville, NY, USA). For motility analysis, the

sperm were tracked using ImageJ, and the trajectories were analysed using GraphPad Prism and an in house MATLAB program.

The swimming speed of sperm was computed using the displacement of the sperm between consecutive images (sampled at 8.17 Hz) and divided by time. The persistence length was computed using the displacement of a trajectory (typically 1.8 s long) divided by the contour length of the trajectory.<sup>13</sup> The x-persistence is the projection of the persistence along the x-axis.<sup>31</sup> Note that the negative direction of the x-axis is the flow direction.

### Reagents and media

Chemicals used in this segment were purchased from Sigma-Aldrich unless otherwise noted. Tyrode Albumin Lactate Pyruvate (TALP),<sup>32</sup> a modified Tyrode balanced salt solution, was used as sperm medium. TALP consisted of 99 mM NaCl, 3.1 mM KCl, 25 mM NaHCO<sub>3</sub>, 0.39 mM NaH<sub>2</sub>PO<sub>4</sub>, 10 mM HEPES free acid, 2 mM CaCl<sub>2</sub>, 1.1 mM MgCl<sub>2</sub>, 25.4 mM sodium lactate, 0.11 mg/mL sodium pyruvate, 5 µg/mL gentamicin, and 6 mg/mL bovine serum albumin (Fraction V; Calbiochem, La Jolla, CA, USA), with a pH of 7.4 and 300 mOsm/kg. TALP was equilibrated in a 38.5 °C incubator with 5% CO<sub>2</sub> in humidified air before use.

### Sperm sample preparation

Semen samples frozen in plastic straws were kindly provided by Genex Cooperative, Inc. (Ithaca, NY, USA). The straws had been diluted in egg yolk extender and frozen according to the standard procedures followed at Genex Cooperative, Inc., which are described in Kaproth *et al.*<sup>33</sup> Procedures to prepare the sperm from the frozen samples are described in Ardon *et al.*<sup>34</sup> Briefly, the straws were first thawed in a 37°C water bath, and then seminal plasma, extender, and dead sperm were removed from live sperm by density gradient centrifugation (300 x g for 10 min)

through two layers (40-80%) of BoviPure diluted in BoviDilute (Spectrum Technologies, Inc., Healdsburg, CA, USA). The sperm pellet was then washed in 3 mL TALP (300 x g, 3 min). Sperm were resuspended in 20  $\mu\text{L}$  of TALP, and kept in an incubator at 38.5 °C under 5%  $\text{CO}_2$  in humidified air until used. Sperm concentration was determined using an improved Neubauer hemacytometer and adjusted to  $10^8$  cells  $\text{mL}^{-1}$ .

## Experimental setup

Prior to running the experiments, the devices were flushed with TALP medium to remove the water in the system. The devices were then submerged under TALP, and equilibrated in a 38.5 °C incubator with 5%  $\text{CO}_2$  in humidified air overnight. During the experiments, the microfluidic devices were kept at 38.5 °C by a temperature-controlled thermal plate (H401-T-BL-LOG, OkoLab, Ottaviano, NA, Italy) and heated stage (TRZ 3700, Carl Zeiss). Sperm suspensions were seeded through the 2 mm hole on the device, and sperm were allowed to swim in with no flow applied. A sperm concentration suitable for the experiments was established in the area shown in Fig. 1C within 3-5 min. Next, different flow rates (0, 1, 3, 5  $\mu\text{L min}^{-1}$ ) were applied in the experiments, and we compared sperm behaviours on flat surfaces with behaviours in the microgrooves. A typical experiment lasted 1-1.5 hr.

## Results and Discussion

### Microfluidic device design and flow characterization

The microfluidic device was designed to recapitulate two main physical features within the mammalian female reproductive tract that are important for directing sperm migration toward the egg: the fluid flow within the main channel and the micro-sized grooves along the surface of the channel. A double layer fabrication method was adopted, in which one layer was fabricated to mimic the main reproductive tract, *i.e.* the main channel, and a second layer contained the micro-

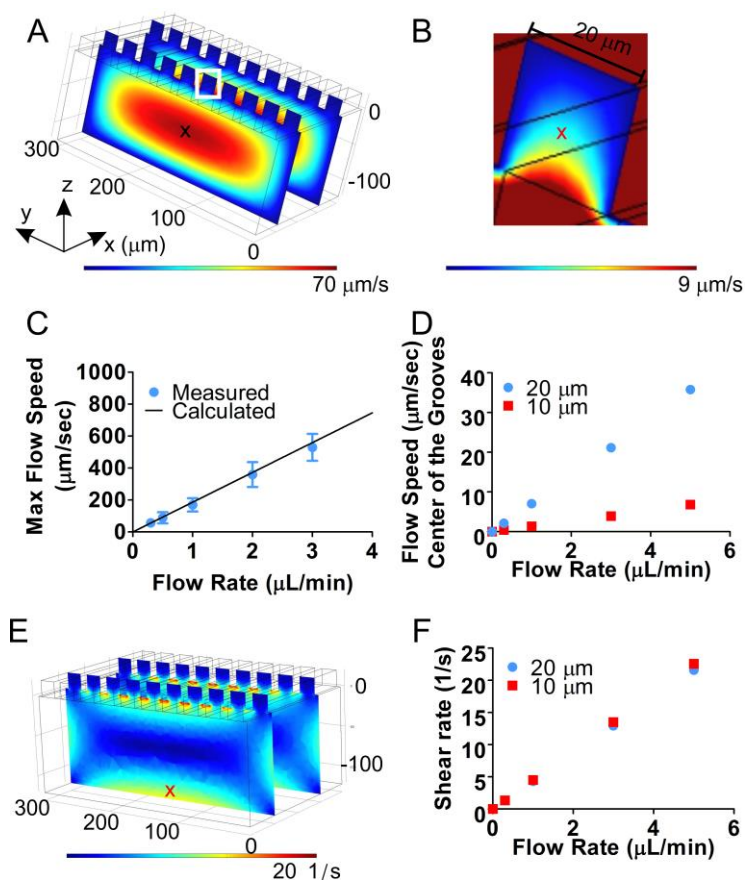


**Fig. 2 Experimental and numerical flow characterization in the microfluidic model.** **A.** Computed flow speed profile within a microfluidic channel ( $300\ \mu\text{m} \times 120\ \mu\text{m}$ ) with  $20\ \mu\text{m} \times 20\ \mu\text{m}$  micro-fabricated grooves on the upper surface. Note that the flow speeds in the micro-fabricated grooves are greatly reduced. **B.** Flow speed profile within one groove as indicated in the white box in A. **C.** Measured flow speed at the centre of the main channel (x in A) using fluorescent particle tracking method is validated against the calculated speed of the same location at various pumping flow rates. **D.** Calculated flow speed at the centre of the grooves (e. g. red x in B) at various pumping flow rates. **E.** Simulation of the shear stress distribution in the microfluidic channel with micro-fabricated grooves. **F.** Shear rate at the bottom and along the mid line (as indicated by the red x shown in E) at various pumping rates.

scale grooves on the surface of the channel (See Fig. 1). For parallel experimentation, 6 separate flow channels were patterned onto a  $\sim 2\ \text{mm}$  thick PDMS layer that was subsequently bonded onto a  $1'' \times 3''$  glass slide, the surface of which was coated with a thin layer of PDMS. All 6 flow channels shared the same cell seeding port and flow input port as shown in Fig. 1A. Each flow channel was  $300\ \mu\text{m}$  wide,  $120\ \mu\text{m}$  deep, and  $8\ \text{mm}$  long. In the middle portion ( $5\ \text{mm}$  long) of the G flow channel (See Fig. 1B), 9 sets of  $20\ \mu\text{m} \times 20\ \mu\text{m}$  cross-section (or 15 sets of  $10\ \mu\text{m} \times 20$

$\mu\text{m}$ ) small grooves were patterned onto the upper PDMS surface. The F channels were free of grooves at the top and served as controls. The details of the groove arrangements are shown in Fig. 1C-D. The small grooves were designed to mimic the microgrooves along the wall of the mammalian female tract, as shown by the image of a frozen tissue section of the bovine cervix in Fig. 1E.

The fluid flow speed within the main channels and surface grooves were characterized and validated using a fluorescent particle tracking method in conjunction with numerical computation. Fig. 2A is a computed flow speed profile within the main channel that has a set of  $20 \times 20 \mu\text{m}$  grooves on the upper surface. A Poiseuille flow profile was reproduced in the main channel, with maximum velocity in the middle of the channel and zero velocity at the boundary. The fluid speed within the groove was significantly slower than that in the main channel, as shown in Fig. 2B. We further measured the flow speed along the mid-line of the main channel (location marked by “x” in Fig. 2A) using a particle tracking method, and validated the measurements against the calculated values using the known pumping rate (See Fig. 2C). Fig. 2D shows that the calculated flow speed along the midline of the groove (marked by “x” in Fig. 2B) was about 30 times slower than those along the midline of the main channel at various pumping rates. Since shear rate was found to play important roles in orienting microswimmers such as bacteria,<sup>22, 35</sup> we computed the spatial distribution of shear rate within the main channel as shown in Fig. 2E. The lowest shear rate was seen within the grooves and in the middle of the main channel; while the highest shear rate was seen on the flat surface and between the grooves. The shear rate (defined as  $\partial u_x / \partial y$ , where  $u_x$  is the streamwise flow velocity,  $y$  is along the depth of the channel) near the bottom of the channel (marked by “x” in Fig. 2E,  $5 \mu\text{m}$  above the surface) is plotted against pumping flow rates in Fig. 2F.

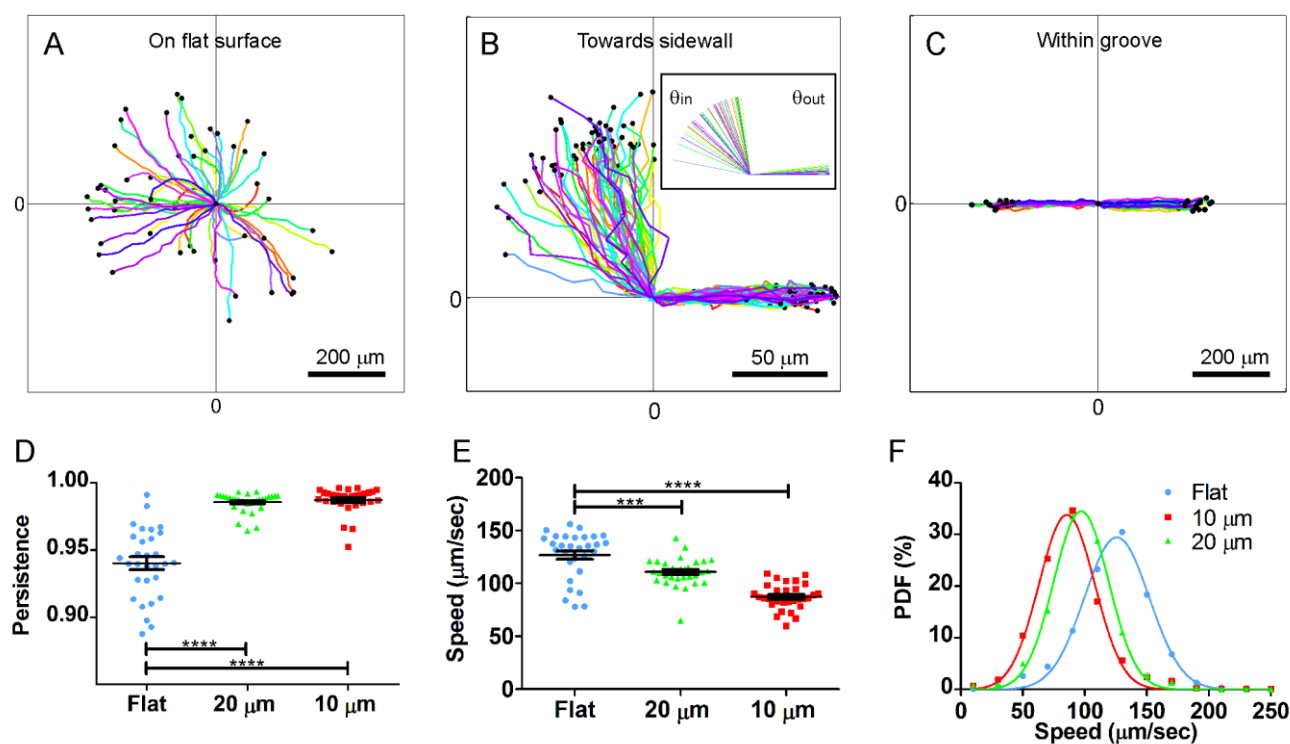


**Fig. 3 Surface topographies guide sperm migration.** A-C. Trajectories of 50 sperm swimming near a flat surface (A), toward a sidewall (B), and within 20  $\mu\text{m}$  x 20  $\mu\text{m}$  grooves (C). Each coloured line is a trajectory of 1.78 s long in A and C, and 1.24 s long in B. The black dots mark both the starting and end points of each trajectory. The coordinate (0,0) marks the starting point of all the tracks in (A,C), and marks the point where the cell hits the side wall in (B). The cells continue move along the sidewall (or along the horizontal axis) once they hit the sidewall. The inset is a graph of the incident ( $\theta_{in}$ ) and outgoing angles ( $\theta_{out}$ ) of the trajectories shown in B. D. Directional persistence is significantly higher for cells travelling within the micro-fabricated grooves than on a flat surface. E. Sperm travelling in the grooves are slower than those on a flat surface. Statistical significances are determined by one-way ANOVA with Bonferroni post test. \*\*\*: p-value < 0.005, \*\*\*\*: p-value < 0.001. Points found outside the mean  $\pm$  3 SD were considered outliers and are not shown (outliers were no more than one point in each data set). F. Speed distribution of sperm swimming on a flat surface and in grooves.

### Surface topographies guide sperm swimming behaviour

Once the sperm were introduced into the cell-seeding inlet (see Fig. 1A), the strong impact of surface topography on sperm swimming behaviour was immediately evident. On a broad flat surface (bottom of the main channel surface), sperm swam mostly along a curved line with no preferred directions as shown in Fig. 3A. As soon as sperm encountered sidewalls, they aligned to

the wall surface and persisted in swimming along it (See Fig. 3B). Once gaining entrance into the micro-fabricated grooves, the sperm swam smoothly and stayed within the grooves (See Fig. 3C).

Microswimmers including sperm have been known to be attracted to a sidewall<sup>14</sup> and to swim along the corner formed by two perpendicular surfaces.<sup>15, 36</sup> Berke *et al.*<sup>37</sup> have observed this phenomenon in swimming bacteria, and attributed it to the hydrodynamic interactions of the swimming bacteria with the flow near the sidewall. Other mechanisms, including the impact/near field lubrication when microswimmers collide with the surface combined with rotational Brownian motion, are also reported to contribute to this swimming behaviour.<sup>38, 39</sup> A noteworthy observation here is that very few sperm came in contact with the sidewall with an incident angle less than 20°. Similar behaviours have been observed for *E. coli* swimming near a surface.<sup>36</sup>

We further quantified swimming behaviour of sperm on a flat surface and within microfabricated grooves using sperm trajectories such as those shown in Fig. 3A and 3C. Clearly, directional persistence of the sperm within grooves was significantly enhanced in comparison to those that swam on large flat surfaces (See Fig. 3D). Persistence is defined as the net displacement (vector length) of a trajectory divided by the contour length of the trajectory.<sup>13</sup> Sperm swimming speed was slowed by the presence of the grooves, likely caused by the fact that grooves restrict the beating amplitude of the sperm. This is further demonstrated by the fact that the sperm swam slower in the narrow groove (width of 10  $\mu\text{m}$ ) than the wide groove (width of 20  $\mu\text{m}$ ). Fig. 3F are the instantaneous speed distribution of the sperm sampled at 8.17 Hz, which shows that the distribution was narrower when they were confined in microfabricated grooves.

### Fluid flow guides sperm swimming direction

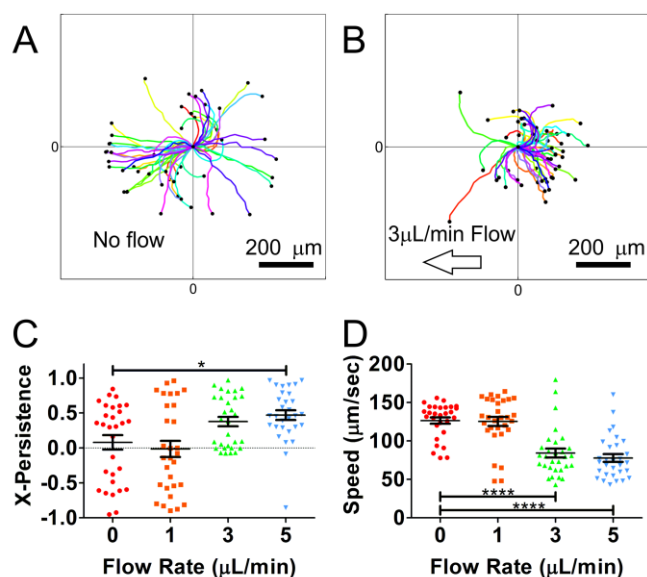


**Fig. 4 Sperm swim against the flow.** **A-B.** Trajectories ( $N=50$ ) of sperm swimming along a flat surface with no flow (**A**), and a  $3 \mu\text{L min}^{-1}$  flow (**B**) within the microfluidic channel. **C.** Persistence along  $x$ -axis direction (opposite to the flow direction) was enhanced in the presence of the high flow (3 and  $5 \mu\text{L min}^{-1}$ ). \*:  $p$ -value  $< 0.05$ , \*\*\*\*:  $p$ -value  $< 0.001$ . **D.** Sperm speed was reduced in the presence of the high flow (3 and  $5 \mu\text{L min}^{-1}$ ).

A high fluid flow (flow rate of  $3 \mu\text{L min}^{-1}$  or  $60 \mu\text{m s}^{-1}$  at the location where the sperm is, or shear rate  $14 \text{ s}^{-1}$  and higher) tended to orient the sperm to swim against the flow (see Fig. 4A-B) when swimming on the lower surface of the channel. In Fig. 4B, about 80% of the cells exhibited motion against the flow of  $3 \mu\text{L min}^{-1}$ . This observation can be quantified by measuring the component of the persistence against the flow direction, as shown in Fig. 4C. Here, the flow is along the negative direction of the  $x$ -axis, and  $x$ -persistence is the  $x$ -component of the net displacement of the trajectory divided by the contour length of the trajectory. In no and low flow ( $0$  and  $1 \mu\text{L min}^{-1}$ ) cases, the average  $P_x$  was close to 0. In high flow ( $3$  and  $5 \mu\text{L min}^{-1}$ ) cases, the average  $P_x$  was close to 0.5. The differential swimming behaviour at low and high flow is also demonstrated by the average sperm swimming speed shown in Fig. 4D.

Aquatic swimmers, such as zebra fish, are known to swim against a flow.<sup>40</sup> Microswimmers, such as bacteria, have been reported to swim against flow. The underlying mechanism for the

microswimmers has been studied extensively and is currently under debate.<sup>22, 35</sup> In one study, the rotation of the flagellum has been found to be important for bacterial rheotaxis.<sup>22, 35</sup> In contrast, some other studies showed that bacteria could achieve rheotaxis as a result of the flow field.<sup>41, 42</sup> Less is known about sperm; however, mammalian sperm have been reported to orient against a flow when swimming on a surface.<sup>5, 43</sup> Since sperm swim via the beating of one flagellum, the present work provides basic data sets for exploring fluid mechanics of a different class of microswimmers in the presence of the flow. We are currently exploring the roles of rotational diffusivity in sperm swimming behaviour in the presence of a flow.

The rationale for our choice of flow rate of  $0 - 5 \mu\text{L min}^{-1}$  (or  $0 - 100 \mu\text{m s}^{-1}$  at the location where the sperm is) is twofold. From the biological perspective, a range is to be expected in the female tract, with flow speed dependent on sporadic muscle contraction,<sup>2</sup> the local concentration of cilia,<sup>44</sup> variation in rate of fluid secretion along the tract,<sup>5</sup> and local microarchitecture. Although *in vivo* measurements of these flow rates are scarce, a speed of  $18.0 \pm 1.6 \mu\text{m s}^{-1}$  was reported to be the average flow speed in mouse oviduct at the time of mating.<sup>5</sup> From a physical science perspective, we chose this flow range because it allowed us to observe a number of different swimming behaviours, including random swimming pattern ( $1 \mu\text{L min}^{-1}$  or less), swimming against flow ( $3 - 5 \mu\text{L min}^{-1}$ ), and being swept away ( $5 \mu\text{L min}^{-1}$  or higher).

### Cooperative roles of micro-fabricated grooves and flow in sperm migration

Fig. 5 shows that micro-fabricated grooves assist sperm in staying on a surface and migrating against a flow. In Fig. 5A1, two sperm in microgrooves were shown to swim against the flow at a steady pace (See also Movie S1). In contrast, sperm swimming on a broad flat surface (Fig. 5A2) struggled to move upstream, nearly halted between frames taken at 245 ms and 367 ms, went

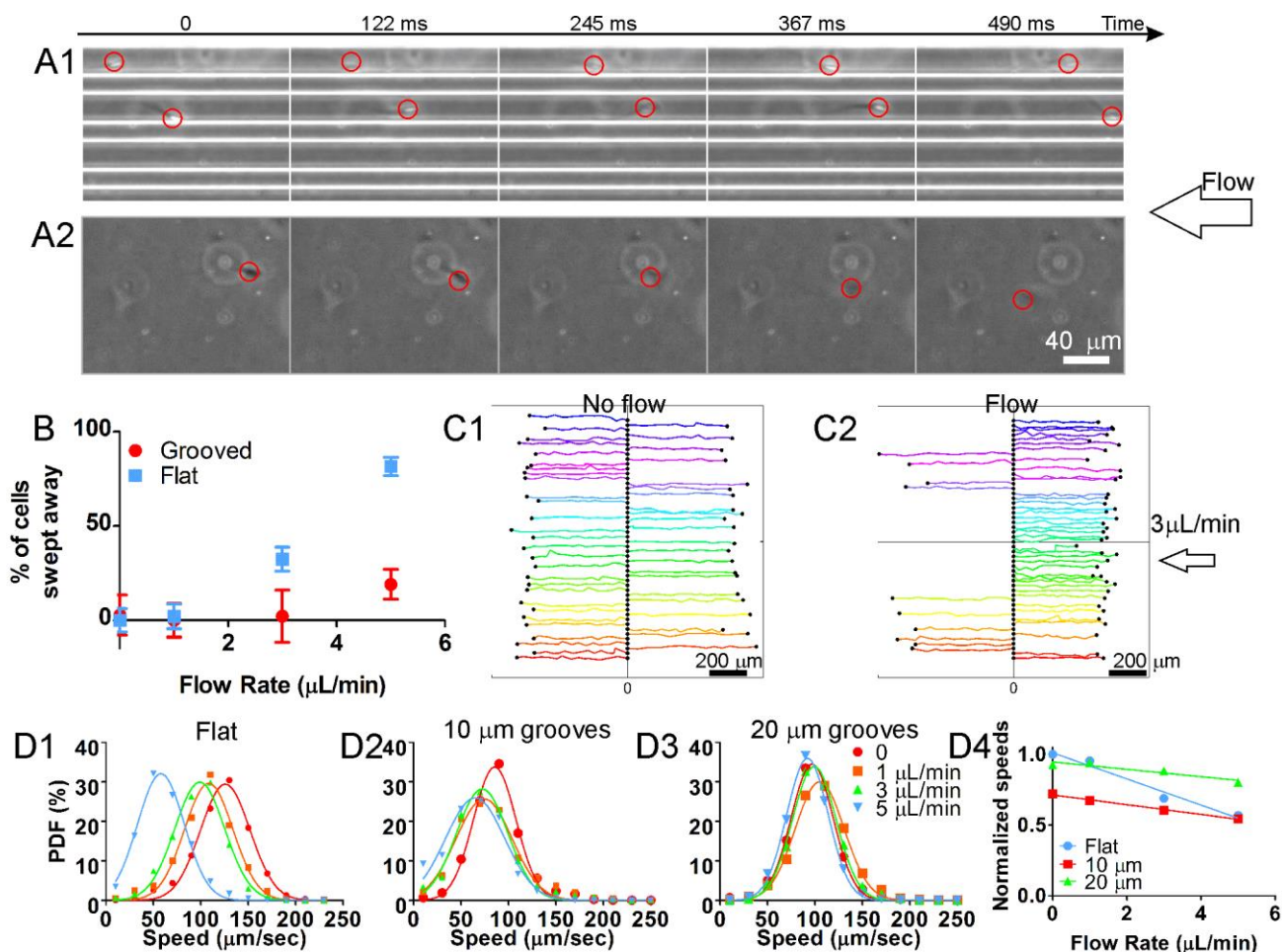


**Fig. 5 Micro-fabricated grooves facilitate sperm migration against the flow.** **A.** Time lapse images of a bull sperm swimming in a  $20\ \mu\text{m} \times 20\ \mu\text{m}$  groove (A1) and on the bottom surface of the microfluidic channel (A2) with a flow rate of  $3\ \mu\text{L}\ \text{min}^{-1}$ . In A2, the cell eventually leaves the surface (becomes out of focus) and is swept downstream. Red circles are used to mark the positions of the sperm head. **B.** Percentage of cells that were swept away by the flow for sperm swimming on flat surfaces or within grooves. **C.** Trajectories of 50 sperm swimming in  $20\ \mu\text{m} \times 20\ \mu\text{m}$  grooves in the absence (C1) and presence (C2) of the flow. The starting point of each trajectory along the x-axis is placed randomly along the y-axis for the ease of visualization of the track direction within the groove. Sperm swim toward both directions nearly equally with no flow, and with a  $3\ \mu\text{L}\ \text{min}^{-1}$  flow, sperm primarily swim against the flow. **D.** Flow influences on sperm swimming speed. Instantaneous sperm speed distribution sampled at  $8.17\ \text{Hz}$  on flat surface (D1) and within grooves (D2-3) at various pumping rates. The dots are experimental data computed from 50 tracks and each track is  $1.78\ \text{s}$  long and the solid lines are fits to Gaussian functions. D4 shows the flow influences on average speed of sperm when swimming on flat surfaces and within micro-fabricated grooves.

downstream at the frame taken at  $490\ \text{ms}$ , and were swept away by the flow afterward (outside of the image sequence shown) (See also Movie S2). Fig. 5B presents the percentage of cells swept downstream by the flow for grooved and flat surfaces at various pumping flow rates. Each data

point was calculated using 4 one-min long movies. Cells that moved from the flat surface to the sidewalls (as shown in Fig. 3B) were excluded for this purpose. At no or low (0 or 1  $\mu\text{L min}^{-1}$ ) flow rates, nearly all of the cells stayed in focus throughout the movie sequence. At 3  $\mu\text{L min}^{-1}$  flow rate,  $32\pm 6\%$  of the cells separated from the flat surface and were swept downstream; in contrast, only  $2\pm 7\%$  of the cells within the 10  $\mu\text{m}$  grooves were swept downstream. At 5  $\mu\text{L min}^{-1}$  flow rate, most sperm were unable to stay on the flat surface, with  $82\pm 5\%$  of the cells being swept downstream by the flow; in contrast, only  $19\pm 8\%$  of the sperm in 10  $\mu\text{m}$  grooves were swept away. It should be noted that the 3  $\mu\text{L min}^{-1}$  corresponds to the shear rate of  $14 \text{ s}^{-1}$  at the surface of the channel.

Sperm tended to swim against the flow when they swam within the micro-fabricated grooves (See Fig. 5C). In this case, we seeded the cells in the cell seeding port, and waited 15 min for the system to reach equilibrium, such that the number of cells swimming toward the left and right was nearly equal (as seen in Fig. 5C1). Fluid flows were then introduced in the flow input port. After one min, the majority of the cells swam against the flow, as shown in Fig. 5C2. We note here that once a cell entered a groove, it was almost certain that it would follow the groove and maintain its swimming direction. Therefore, the preferential swimming direction seen in Fig. 5C2 reflects the preferential directional entry into the grooves. For the thousands of cells we tracked, only one cell was observed to turn around within a groove.

Sperm swimming speed was nearly unaltered in the presence of the flow when swimming within grooves, as shown in Fig. 5D. Again, this shows that microgrooves assisted sperm to swim against the flow. Fig. 5D1 shows that sperm speed decreased with increased flow rate when sperm were swimming on a flat surface. Fig. 5D1 was obtained by computing the distribution of

instantaneous speeds of 50 cells, sampled at 8.17 Hz from a 1.8 s movie. In the case of sperm swimming within grooves, the speed distribution was nearly unaltered in the presence of the flow. This tendency was also reflected in the average speed of sperm swimming on flat and grooved surfaces (See Fig. 5D4). Note that we normalized all speed data to the average speed on a flat surface under no flow condition in Fig. 5D4. All speed measurements were done at the laboratory reference frame.

Here, the microfluidic *in vitro* model enabled us to study the cooperative effects of surface topographies and fluid flows on sperm cell migration. First, it showed that microgrooves assist the sperm in staying on a surface; second, it showed that microgrooves facilitated sperm swimming against the mainstream flow. This indicates that the microgrooves that are present along the female reproductive tract, particularly in the cervix and uterotubal junction, have evolved to provide sperm with the ability to swim against the general fluid flow. Such findings may shed light on the design of devices for successful *in vitro* fertilization<sup>28, 43</sup> and for designing contraceptives that minimize the use of pharmacological agents by using microarchitecture to direct sperm movement away from the path to the egg.

## Conclusions

We present here a microfluidic model for recreating the biophysical environment of mammalian sperm. Using bull sperm as a model system, we found that (1) micro-fabricated grooves on a surface assist sperm in staying at the surface in the presence of a flow; (2) the microgrooves allow sperm to swim faster and more efficiently in the presence of the flow, in contrast to those swimming on a flat surface; and (3) sperm orient themselves against a flow when the flow shear rate exceeds  $14 \text{ s}^{-1}$ . The microfluidic model opens the door for quantitative studies of biophysical

parameters that regulate mammalian sperm migration, and may have direct implications for the design of *in vitro* fertilization devices and for the development of new contraceptives that use microarchitecture to entrap sperm. In addition, this microfluidic device can easily be adapted to study the roles of surface topography and flow in the movement of other microswimmers, such as bacteria. Lastly, such devices would have direct applications to commercial bioprocesses such as biofuel production. Currently, we are using this device to study the mechanisms of migration of disease-causing microswimmers that infect the female reproductive tract.

## Acknowledgements

This work was supported by the National Institutes of Health (NIH) 1R01HD070038, and performed in part at the Cornell Nanobiotechnology Center (NBTC) and the Cornell NanoScale Science and Technology (CNF).

## Notes and references

<sup>a</sup> Department of Biological and Environmental Engineering, Cornell University, Ithaca, NY, USA. Email: mw272@cornell.edu

<sup>b</sup> Department of Biomedical Sciences, Cornell University, Ithaca, NY, USA. Email: sss7@cornell.edu

†

Electronic Supplementary Information (ESI) available. See DOI: 10.1039/b000000x/

1. K. June Mullins and R. G. Saacke, *The Anatomical Record*, 1989, **225**, 106-117.
2. S. S. Suarez and A. A. Pacey, *Human Reproduction Update*, 2006, **12**, 23-37.
3. E. A. Gaffney, H. Gadêlha, D. J. Smith, J. R. Blake and J. C. Kirkman-Brown, *Annual Review of Fluid Mechanics*, 2011, **43**, 501-528.
4. S. S. Suarez, K. Brockman and R. Lefebvre, *Biology of Reproduction*, 1997, **56**, 447-453.
5. K. Miki and D. E. Clapham, *Current Biology*, 2013, **23**, 443-452.
6. S. S. Suarez, D. F. Katz, D. H. Owen, J. B. Andrew and R. L. Powell, *Biology of Reproduction*, 1991, **44**, 375-381.
7. A. Cohen-Dayag, I. Tur-Kaspa, J. Dor, S. Mashlach and M. Eisenbach, *Proceedings of the National Academy of Sciences*, 1995, **92**, 11039-11043.
8. G. Fabro, R. A. Rovasio, S. Civalero, A. Frenkel, S. R. Caplan, M. Eisenbach and L. C. Giojalas, *Biology of Reproduction*, 2002, **67**, 1565-1571.
9. F. Sun, A. Bahat, A. Gakamsky, E. Girsh, N. Katz, L. C. Giojalas, I. Tur-Kaspa and M. Eisenbach, *Human Reproduction*, 2005, **20**, 761-767.
10. U. B. Kaupp, N. D. Kashikar and I. Weyand, *Annual Review of Physiology*, 2008, **70**, 93-117.
11. U. B. Kaupp, *The Journal of General Physiology*, 2012, **140**, 583-586.
12. M. V. Inamdar, T. Kim, Y.-K. Chung, A. M. Was, X. Xiang, C.-W. Wang, S. Takayama, C. M. Lastoskie, F. I. M. Thomas and A. M. Sastry, *Journal of Experimental Biology*, 2007, **210**, 3805-3820.
13. H. Chang, B. J. Kim, Y. S. Kim, S. S. Suarez and M. Wu, *PLOS ONE*, 2013, **8**, e60587.
14. Rothschild, *Nature*, 1963, **198**, 1221.
15. P. Denissenko, V. Kantsler, D. J. Smith and J. Kirkman-Brown, *Proceedings of the National Academy of Sciences of the United States of America*, 2012, **109**, 8007-8010.

16. V. Kantsler, J. Dunkel, M. Polin and R. E. Goldstein, *Proceedings of the National Academy of Sciences of the United States of America*, 2013, **110**, 1187-1192.
17. M. d. C. Lopez-Garcia, R. L. Monson, K. Haubert, M. B. Wheeler and D. J. Beebe, *Biomedical Microdevices*, 2008, **10**, 709-718.
18. J. Cosson, P. Huitorel and C. Gagnon, *Cell Motility and the Cytoskeleton*, 2003, **54**, 56-63.
19. D. J. Smith, E. A. Gaffney, J. R. Blake and J. C. Kirkman-Brown, *Journal of Fluid Mechanics*, 2009, **621**, 289-320.
20. J. Elgeti, U. B. Kaupp and G. Gompper, *Biophysical Journal*, 2010, **99**, 1018-1026.
21. Y.-A. Chen, Z.-W. Huang, F.-S. Tsai, C.-Y. Chen, C.-M. Lin and A. Wo, *Microfluidics and Nanofluidics*, 2011, **10**, 59-67.
22. J. Hill, O. Kalkanci, J. L. McMurry and H. Koser, *Physical Review Letters*, 2007, **98**.
23. L. I. Segerink, A. J. Sprenkels, P. M. ter Braak, I. Vermees and A. van den Berg, *Lab on a Chip*, 2010, **10**, 1018-1024.
24. R. S. Suh, X. Zhu, N. Phadke, D. A. Ohl, S. Takayama and G. D. Smith, *Human Reproduction*, 2006, **21**, 477-483.
25. D. Petrin, K. Delgaty, R. Bhatt and G. Garber, *Clinical Microbiology Reviews*, 1998, **11**, 300-317.
26. V. Midlej, R. Vilela, A. B. Dias and M. Benchimol, *Veterinary Parasitology*, 2009, **165**, 216-230.
27. D. Lai, G. D. Smith and S. Takayama, *Journal of Biophotonics*, 2012, **5**, 650-660.
28. J. E. Swain, D. Lai, S. Takayama and G. D. Smith, *Lab on a Chip*, 2013, **13**, 1213-1224.
29. S. G. Clark, K. Haubert, D. J. Beebe, C. E. Ferguson and M. B. Wheeler, *Lab on a Chip*, 2005, **5**, 1229-1232.
30. C. Han, Q. Zhang, R. Ma, L. Xie, T. Qiu, L. Wang, K. Mitchelson, J. Wang, G. Huang, J. Qiao and J. Cheng, *Lab on a Chip*, 2010, **10**, 2848-2854.
31. B. J. Kim, P. Hannanta-anan, M. Chau, Y. S. Kim, M. A. Swartz and M. Wu, *PLoS ONE*, 2013, **8**, e68422.
32. J. J. Parrish, J. Susko-Parrish, M. A. Winer and N. L. First, *Biology of Reproduction*, 1988, **38**, 1171-1180.
33. M. T. Kaproth, H. E. Rycroft, G. R. Gilbert, G. Abdel-Azim, B. F. Putnam, S. A. Schnell, R. W. Everett and J. E. Parks, *Theriogenology*, 2005, **63**, 2535-2549.
34. F. Ardon and S. S. Suarez, *Reproduction*, 2013, **146**, 111-117.
35. Marcos, H. C. Fu, T. R. Powers and R. Stocker, *Proceedings of the National Academy of Sciences of the United States of America*, 2012, **109**, 4780-4785.
36. P. Galajda, J. E. Keymer, P. M. Chaikin and R. H. Austin, *Journal of Bacteriology*, 2007, **189**, 8704-8707.
37. A. P. Berke, L. Turner, H. C. Berg and E. Lauga, *Physical Review Letters*, 2008, **101**, 038102.
38. G. Li and J. X. Tang, *Physical Review Letters*, 2009, **103**, 078101.
39. K. Drescher, J. Dunkel, L. H. Cisneros, S. Ganguly and R. E. Goldstein, *Proceedings of the National Academy of Sciences*, 2011, **108**, 10940-10945.
40. A. Suli, G. M. Watson, E. W. Rubel and D. W. Raible, *PLOS ONE*, 2012, **7**, e29727.
41. R. W. Nash, R. Adhikari, J. Tailleur and M. E. Cates, *Physical Review Letters*, 2010, **104**.
42. T. Brotto, J.-B. Caussin, E. Lauga and D. Bartolo, *Physical Review Letters*, 2013, **110**, 038101.
43. D. B. Seo, Y. Agca, Z. C. Feng and J. K. Critser, *Microfluidics and Nanofluidics*, 2007, **3**, 561-570.
44. H. Chang and S. S. Suarez, *Biology of Reproduction*, 2012, **86**, 140, 141-148.